Journal of Sound and Vibration 607 (2025) 119064

Contents lists available at ScienceDirect

Journal of Sound and Vibration

journal homepage: www.elsevier.com/locate/jsvi

On the zero frequency bandgap of seismic metamaterials

Jingyu Luo [a,b], Kaiming Bi [a,b,*], Xingbo Pu [a,c,*]

[a] Department of Civil and Environmental Engineering, The Hong Kong Polytechnic University, Kowloon, Hong Kong, China
[b] Research Centre for Urban Hazards Mitigation (RCUHM), The Hong Kong Polytechnic University, Kowloon, Hong Kong, China
[c] Joint Research Centre for Marine Infrastructure, The Hong Kong Polytechnic University, Kowloon, Hong Kong, China

ARTICLE INFO

Keywords:
Seismic metamaterial
Zero-frequency bandgap
Mechanism
Misconception

ABSTRACT

Seismic metamaterials are artificially designed materials within the sub-wavelength range, developed to attenuate low-frequency seismic surface waves. Previous studies revealed that through proper design, a zero-frequency bandgap (ZFBG) can be formed. However, the underlying mechanism for forming the ZFBG has not been well explained so far. Many existing studies attributed it to the collective behavior of the individual unit cells within the metamaterial. In this work, we clarify that the ZFBG is not exclusive to metamaterials. We investigate the mechanism of ZFBG by revisiting two typical designs: clamped barriers and resonant meta-barriers. Through analytical and numerical analyses, we claim that the ZFBG of the former design lies in the cut-off frequency originating from the rigid boundary condition, while the latter design is due to an intrinsic property of having a stiff upper layer atop a soft half-space, which cannot support low-order surface wave modes. This work corrects a misconception in this field and thus could facilitate the understanding, design, and implementation of seismic metamaterials.

1. Introduction

In recent decades, research on metamaterials, engineered composite materials or structures, has led to a variety of promising applications across multiple fields, including physics, mechanics, engineering, and information science. Despite differences in spatial and frequency ranges, these materials are characterized by their ability to manipulate waves through carefully designed unit cells [1, 2]. This capability enables functions such as wave cloaking, super-resolution imaging, waveguiding, signal sensing, and wave splitting [3–5].

Among these advancements, seismic metamaterials have emerged as an innovative method for controlling and redirecting seismic energy from seismic events [6–8]. These materials possess bandgap properties that inhibit elastic wave propagation within specific frequency ranges. This innovation is particularly attractive in civil engineering, where the control of low-frequency elastic waves especially surface waves (Rayleigh and Love waves) is of great importance because they carry the majority of elastic energy along the soil surface.

Initially, surface-wave bandgaps were created using multiple rows of boreholes, infilled trenches, and piles. With proper design, these metamaterials can achieve a wide bandgap of around 50 Hz [9], making them appealing for controlling ambient vibrations from sources like railways and machinery [10–12]. However, challenges remain for seismic surface wave isolation due to Bragg's law, which

* Corresponding authors at: Department of Civil and Environmental Engineering, The Hong Kong Polytechnic University, Kowloon, Hong Kong, China.
E-mail addresses: kaiming.bi@polyu.edu.hk (K. Bi), xingbo.pu@polyu.edu.hk (X. Pu).

https://doi.org/10.1016/j.jsv.2025.119064
Received 20 November 2024; Received in revised form 25 February 2025; Accepted 12 March 2025
Available online 13 March 2025

necessitates destructive interference of waves at wavelengths comparable to the spatial periodicity of the lattice [13–15]. Motivated by the development of locally resonant metamaterials [16], researchers have revisited the reduction of surface wave amplitude through the interaction between surface motion and localized resonator modes [17,18]. These meter-sized resonant devices, either buried in or positioned above the soil around target structures, function similarly to multiple tuned-mass dampers. They can create surface wave bandgaps at the resonators' natural frequencies. Their interaction can also be leveraged to adjust the phase velocities and wavelengths of propagating surface waves, providing additional opportunities for surface wave control. Indeed, these unique capabilities have been both predicted and observed in various natural and artificial seismic metamaterials, including forests of trees [19], rows of resonant wave barriers [20–22], and metawedges [23,24]. While these seismic metamaterials can create Hertz-level bandgaps, taking an important step towards the control of seismic waves, the width of the bandgap is often relatively narrow compared to the Bragg bandgap, which limits their engineering applications.

The aforementioned challenge has been partially addressed by advanced designs of seismic metamaterials that enable ultra-low-frequency and even zero-frequency bandgaps (ZFBGs) [25–27]. Typically, a periodic array of concrete columns clamped at their bases to the bedrock can achieve a wide bandgap starting from 0 Hz [28–30], as shown in Fig. 1a. This concept has recently evolved into a novel class of embedded seismic metamaterials, consisting of steel piles periodically clamped onto a concrete base [31], specifically designed to overcome the need for substantial dimensions when inserting into the bedrock. In parallel, ZFBGs have also been found using meter-sized plate-like unit cells placed on a half-space [32,33], as depicted in Fig. 6a. These unit cells often feature cross-like cavities and/or inclusions embedded in a hard matrix, resulting in a high impedance ratio between the metamaterial and the soil half-space. Since this type of seismic metamaterial does not require bedrock or a rigid base to support the bottom of the pillars, it offers an ideal alternative for specific site conditions, particularly in soft soil regions where the bedrock is notably deep.

Despite these pioneering contributions that have significantly advanced the field of seismic metamaterials, the underlying mechanism for the formation of ZFBGs remains inadequately explained. Most previous studies suggested that ZFBGs in clamped seismic metamaterials arise from the strong constraints between the piles and the surrounding soil, while those in meta-barriers are attributed to the negative effective mass density of the metamaterial plate. While these conclusions hold some validity, they do not fully elucidate the underlying mechanism. In fact, classical soil dynamics [34] indicate that when a harmonic load is applied to the surface of a single soil layer over bedrock, a cutoff frequency exists for the forced vibration of that soil layer. If the frequency of the harmonic load falls below this cutoff frequency, wave propagation within the soil layer will not occur. It is important to note that no periodic pillars are introduced in the soil in this scenario, so it cannot be classified as a seismic metamaterial; however, the resulting phenomenon aligns with the clamped seismic metamaterial. Additionally, classical soil dynamics [34] also demonstrate that when a stiff soil layer overlies a soft soil layer, low-order surface wave modes do not exist. While this scenario does not involve the introduction of metamaterials neither, the outcomes are reminiscent of the ZFBG in the meta-barrier.

Hence, in this work, we aim to clarify the mechanisms behind the formation of ZFBGs in seismic metamaterials. To achieve this, we revisit the two representative models mentioned above, namely the clamped barrier model and the resonant meta-barrier model. We develop a discrete model to analytically demonstrate the physical origin of the ZFBG in the clamped barrier model. Additionally, we validate this mechanism by numerically calculating the dispersion relation and analyzing responses in both the frequency and time domains. Proceeding in a similar fashion, we clarify the ZFBG mechanism for the resonant meta-barriers as well.

This paper is organized as follows: In Section 2, we present both analytical and numerical models to investigate the ZFBG of the clamped barrier model. Section 3 continues this exploration by elucidating the ZFBG mechanism for resonant meta-barriers. Finally, we summarize the main conclusions of our work in Section 4.

2. Clamped barrier model

This section examines the mechanism behind the ZFBG in a clamped barrier design within a two-dimensional plane strain framework. We analyze the standard trench barriers, each measuring 0.2 m in width and 5 m in depth, constructed from conventional

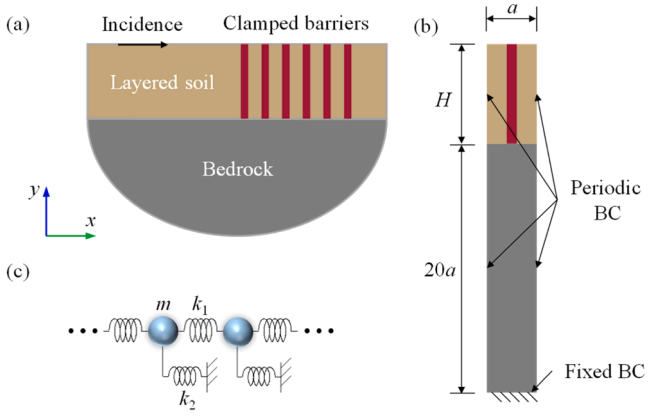

Fig. 1. Schematic diagram of: (a) Continuum model, (b) Unit cell model and (c) Discrete model of clamped barrier design.

fly ash material. These clamped barriers are situated in layered soil above a bedrock half-space, as shown in Fig. 1a. We further assume that these barriers are anchored to the bedrock and arranged periodically with a spacing of $a = 1$ m along the x-direction, as illustrated in the unit cell in Fig. 1b. Further, the fully fixed boundary condition is located at the bottom edge of the model. Due to the significantly higher stiffness of the bedrock compared to the overlying soil layers, the bedrock equivalently imposes a fixed constraint on the upper soil layer. Additionally, all materials involved are treated as linear elastic, homogeneous, and isotropic. Table 1 tabulates the material properties. It should be noted that rubber will be used in Section 3, it is also included in this table.

2.1. Analytical analysis

We start our discussion with a straightforward analytical model, aiming to uncover the underlying physics. To simplify the analysis, we here focus on the long wavelength limit and consider only horizontal wave motion, as the vertical motion is decoupled in our linear system. Based on these assumptions, the system shown in Fig. 1a can be represented by the discrete model in Fig. 1c [35]. In this model, the unit cells consist of identical masses m separated by a distance of a. The presence of bedrock is represented by a fixed boundary condition at the base of the cells. Therefore, in addition to the internal interactions modeled by linear elastic Hooke's springs k_1, the cells also include grounded springs k_2. The stiffness of k_1 represents the soil stiffness between adjacent barriers, while k_2 models the lateral stiffness of the clamped barrier. While this simplified theoretical model does not fully capture the continuum representation shown in Fig. 1a, it is adequate to capture the essential physical principles of the continuum system.

The equation governing the displacement of the n-th cell reads:

$$m\ddot{u}_n + k_1(2u_n - u_{n+1} - u_{n-1}) + k_2 u_n = 0. \tag{1}$$

Based on the Bloch theorem [36], the displacement solution of the n-th unit cell is given by:

$$u_n = U e^{\mathrm{i}(nka-\omega t)}, \tag{2}$$

where k is the wave vector, ω is the angular frequency, $\mathrm{i} = \sqrt{-1}$ is the imaginary unit, and U is the displacement amplitude.

Substituting Eq. (2) into Eq. (1) yields the dispersion relation of the current discrete model:

$$\cos ka = 1 - \frac{m_{eff}\omega^2}{2k_1}, \tag{3}$$

where the effective mass [37] of the unit cell reads:

$$m_{eff} = m - \frac{k_2}{\omega^2} \tag{4}$$

From Eq. (4), we can draw two key observations: (i) First, in the ultra-low-frequency region, the effective mass becomes negative, leading to a stop band that prohibits wave propagation. The cutoff frequency for this stop band occurs at $\omega = \sqrt{k_2/m}$. (ii) Second, when considering a homogeneous soil layer over bedrock, namely without the presence of clamped barriers, the stop band still exists, but its cutoff frequency is lower than that of the clamped barrier system due to the softening of the grounded spring k_2. This indicates that the stop band arises from the rigid bottom boundary condition rather than from the seismic metamaterials (clamped barriers). We will validate these preliminary observations through numerical studies in what follows.

2.2. Numerical analysis

2.2.1. Dispersion relation

In this section, we study the dispersion relation of the proposed two-dimensional (2D) clamped barrier model shown in Fig. 1a. The governing equation for in-plane waves is described as follows [38]:

$$\rho\ddot{u} = \frac{E}{2(1+\nu)}\nabla^2 u + \frac{E}{2(1+\nu)(1-2\nu)}\nabla(\nabla\cdot u) \tag{5}$$

where $\mathbf{u} = (u,\ w)$ is the displacement vector; E, ν, and ρ are the Young's modulus, the Poisson's ratio, and the density of the materials, respectively. ∇ represents the differential operator.

The dispersion relations are constructed by performing eigenfrequency analyses on a unit cell shown in Fig. 1b. To simulate the

Table 1
Material parameters.

Material	ρ (kg/m^3)	E (Pa)	ν
Soil	1800	2e7	0.3
Fly ash	500	2.5e7	0.35
Rubber	1300	1.2e5	0.47
Concrete	2500	3e10	0.3
Bedrock	2800	1e11	0.3

dynamics of an infinite array of periodic clamped barriers, we apply Bloch periodic boundary conditions (BCs) to the vertical substrate edges of the unit cell. This allows us to derive a standard second-order eigenvalue equation:

$$(\mathbf{K}(k) - \omega^2\mathbf{M})\mathbf{U} = 0 \tag{6}$$

where **K** is the stiffness matrix, **M** is the mass matrix, and **U** is the displacement column vector at all nodes.

We develop a finite element (FE) model and numerically solve Eq. (6) using the commercially available software COMSOL Multiphysics. To distinguish surface modes from bulk modes, we define the parameter ξ [39], which depicts the energy distribution of a considered wave mode in this system, based on the center of the displacement fields along the *y*-axis:

$$\xi = \frac{\int_\Omega y(uu^* + ww^*)\mathrm{d}S}{H\int_\Omega (uu^* + ww^*)\mathrm{d}S} \tag{7}$$

in which the asterisk (*) as a superscript indicates the complex conjugate, H is the substrate height, and Ω denotes the whole domain of the substrate. It can be seen from Eq. (7) that the parameter ξ ranges from 0 to 1. Specifically, a value of ξ close to 1 indicates that the energy center is near the free surface, signifying a surface mode. In contrast, a value approaching 0 suggests a bulk mode.

Assuming the mechanical parameters in Table 1, the numerical dispersion curves are obtained by solving the eigenvalue problem for wave vector in the range of ($k = [0,\ \pi/a]$) as shown in Fig. 2a. For comparison, we also analyze the dispersion relation of a unit cell model without clamped barriers, consisting solely of soil and bedrock, as shown in Fig. 2b. As anticipated, the eigen-solutions of both models are similar, as evidenced by the dispersion curves and typical mode shapes presented in the insets (*A*-*H*). Notably, both models exhibit a stop band; however, the cutoff frequencies differ: 3.6 Hz for the clamped barrier model and 3.3 Hz for the bedrock model without clamped barriers. This discrepancy, as explained by the analytical solution in Eq. (4), arises from the introduction of clamped barriers, which increase the overall stiffness of the system. Based on the comparison of the eigen-solutions, we conclude that the ZFBG arises from the rigid boundary condition rather than from the dynamic interaction of the metamaterial itself. We will further elaborate on this conclusion in the subsequent discussion by examining the frequency and time domain analyses.

2.2.2. *Frequency domain analysis*

To further evidence our findings regarding the ZFBG revealed by the dispersion analysis, we conduct FE numerical simulations in the frequency domain. Here, we consider an array of six clamped barriers arranged periodically with a distance of *a*. Additional geometric parameters are detailed in Fig. 3.

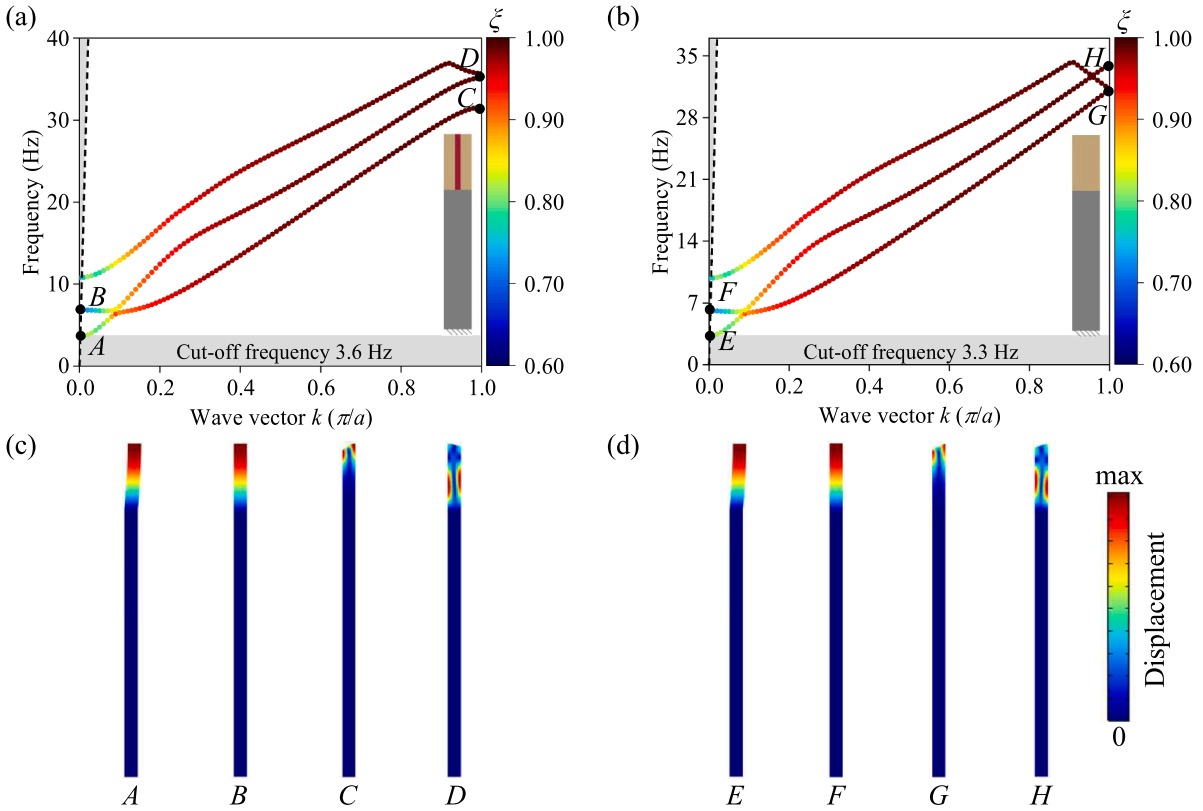

Fig. 2. Dispersion curve of (a) Clamped barrier model and (b) Bedrock model. Typical modes of (c) Clamped barrier model and (d) Bedrock model.

The incident surface waves are generated by a horizontal harmonic point load positioned sufficiently far from the clamped barriers. To simulate the half-space and minimize unwanted reflected waves, we apply perfectly matched layers (PMLs) to the vertical and bottom edges of the model. The substrate domain is discretized into quadrilateral elements utilizing quadratic Lagrange shape functions. To ensure a convergent solution at the highest frequency of interest, the minimum mesh dimension is set to $\lambda/8$, where λ is the wavelength of the incident wave.

To quantify the attenuation effect, the amplitude ratio spectrum (ARS) is defined:

$$ARS = 20\log_{10}(A_1/A_0) \tag{8a}$$

$$ARS = 20\log_{10}(A_2/A_0) \tag{8b}$$

where A_1 and A_2 are the displacement amplitudes of the output point with and without clamped barriers, respectively; A_0 is the amplitude of the pure soil (i.e., without bedrock) selected for comparison purposes.

Fig. 4a illustrates the ARS in the low-frequency range of 0-5 Hz. Notably, from 0 Hz to 3.3 Hz (indicated by the shaded area), the ARS for models with and without clamped piles is negative. This suggests that incident Rayleigh waves within this frequency range are attenuated in both models, as further supported by the horizontal wavefield comparisons shown in Fig. 4b and 4c.

Importantly, this frequency range corresponds to the stop band identified in Fig. 2. Additionally, the ARS for both models aligns within this range, indicating that the introduction of the barrier row does not enhance the attenuation of Rayleigh waves below the cutoff frequency. This observation reinforces our conclusion that the stop band is not an intrinsic characteristic of the metamaterials, but rather a consequence of the fully fixed boundary conditions. Consequently, a superimposed stop band can be achieved through appropriate model design, as detailed in Appendix A.

2.2.3. *Time domain analysis*

In this section, we conduct a time transient analysis to further validate our conclusions. To achieve this, we excite Rayleigh waves using a time-dependent signal, as described in [40], which is given by:

$$F_{in}(t) = F\left[D(t) - D\left(t - \frac{10}{f_c}\right)\right]\left[1 - \cos\left(\frac{2\pi f_c t}{10}\right)\right]\sin(2\pi f_c t) \tag{9}$$

where F, t, $D(t)$, and f_c are the amplitude of the signal, time, Heaviside step function, and central frequency of the signal, respectively.

To evaluate the wave mitigation performance, we consider an incident signal with a central frequency of $f_c = 2$ Hz induced by a horizontal harmonic point load, which falls within the range of the ZFBG. Similarly, the horizontal displacement at the output point is recorded, and a homogeneous half-space model consisting solely of soil is used for comparison.

The results are presented in Fig. 5a. As anticipated, both models, namely those with and without clamped barriers, exhibit a significant attenuation effect, with negligible discrepancies between them (as shown in the zoomed-in results). To further illustrate the attenuation effect in the time domain, Figs. 5b and 5c display snapshots of the horizontal wavefield at $t = 8$ s, which show good agreement. Overall, the time-dependent analysis reinforces the conclusion that the ZFBG arises from the fully fixed boundary condition rather than from the metamaterial itself.

3. Resonant meta-barrier model

In this section, we investigate the mechanism of another typical resonant meta-barrier design that can form ZFBG. Fig. 6a shows the unit cell of the resonant meta-barrier, which consists of a rubber-coated concrete block embedded in a concrete matrix atop a soil half-space. The geometric parameters of the unit cell are $L = 1.0$ m, $l_1 = 0.8$ m, $l_2 = 0.6$ m, $l_3 = 0.5$ m and the material parameters are illustrated in Table 1. We assume that these unit cells are periodically arranged along the x-direction, with a lattice space $a = L = 1.0$ m, suggesting that the outer concrete box of each cell is perfectly bonded.

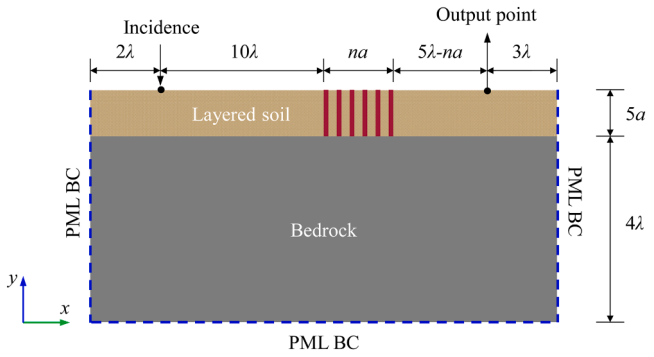

Fig. 3. Schematic of the finite element model for calculating attenuation effect.

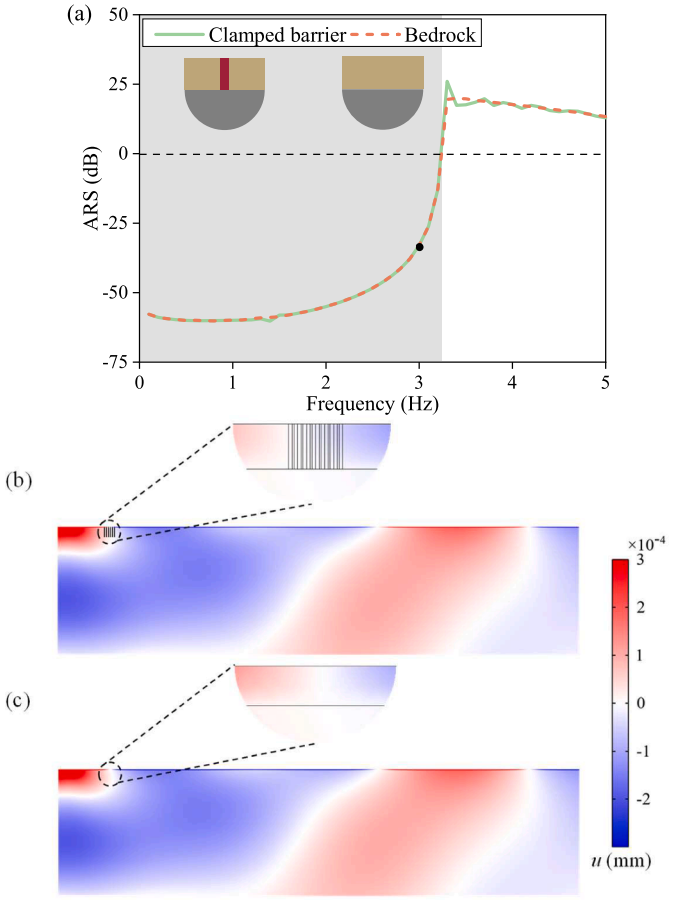

Fig. 4. Frequency domain results. (a) ARS spectrum. Horizontal displacement field of (b) Clamped barrier model and (c) Bedrock model.

3.1. Analytical analysis

Before we begin any quantitative analysis, let us recall Rayleigh wave propagation in a homogeneous layered half-space to better understand the meta-barrier issue. To this end, we focus on the long wavelength limit and consider scenarios that are not near the resonant frequency of the resonator. This allows us to ignore geometric scattering and significant dispersive effects. Consequently, we can model the meta-barrier layer as a uniform concrete layer. The problem can then be framed as analyzing the dynamics of surface Rayleigh waves in a layered half-space consisting of a hard upper layer and a soft substrate, as shown in Fig. 6b.

According to the classical elastic wave theory [41], the potential functions of harmonic surface waves in the substrate are written as:

$$\varphi = \widetilde{B}_1 e^{p_2 y} e^{i(\omega t - kx)} \tag{10a}$$

$$\psi_y = \widetilde{B}_2 e^{q_2 y} e^{i(\omega t - kx)} \tag{10b}$$

$$p_2 = \sqrt{k^2 - \frac{\omega^2}{C_{P2}^2}},\ q_2 = \sqrt{k^2 - \frac{\omega^2}{C_{S2}^2}} \tag{11}$$

where $\widetilde{B_1}$, $\widetilde{B_2}$ are the amplitudes of the potentials; $k = \omega / C_R$ is the wave vector of the Rayleigh wave; ω is the angular frequency; C_R is the Rayleigh-wave velocity; C_{P2} and C_{S2} represent the velocity of pressure and shear waves in the substrate soil, respectively. It is important to note that for a propagating Rayleigh wave, both wavenumbers p_2 and q_2 must be real values.

In principle, the phase velocity of propagating Rayleigh waves is slightly lower than that of shear waves. In layered media, the phase velocity of Rayleigh waves falls between the shear wave phase velocities of the upper and lower layers. In our model, the phase velocity of propagating Rayleigh waves, if it exists, should satisfy the following condition:

$$C_{S2} < C_R < C_{S1} \tag{12}$$

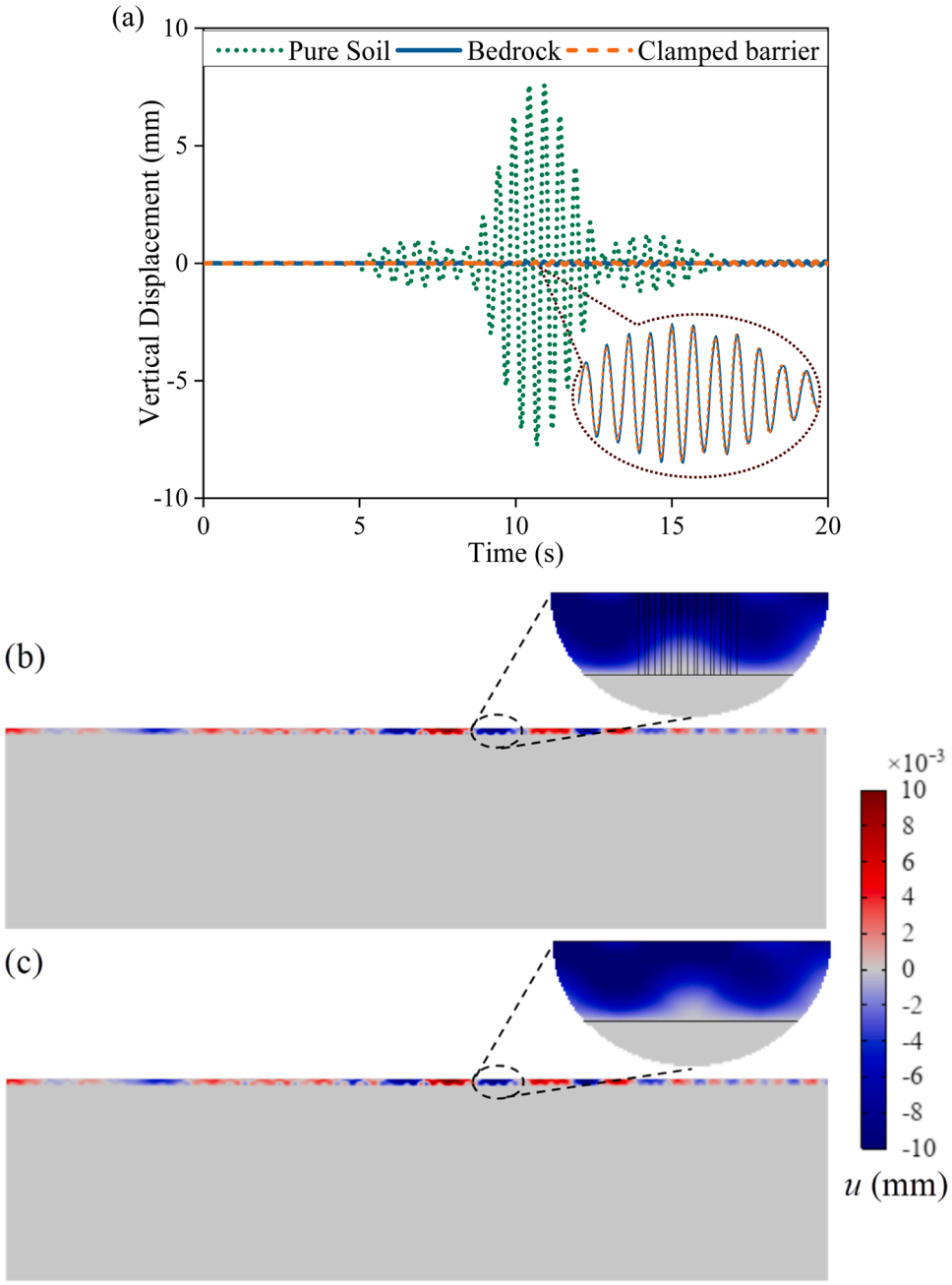

Fig. 5. Time domain results. (a) Horizontal displacement time history. Horizontal displacement field of (b) Clamped barrier model and (c) Bedrock model.

By revisiting Eq. (11), we find that this condition leads to both p_2 and q_2 becoming complex numbers. This indicates that the considered model does not support pure Rayleigh wave modes; instead, only pseudo-surface waves and/or body waves are present. Next, we will verify these qualitative explanations using numerical simulations.

3.2. Numerical model

3.2.1. Dispersion relation

In this section, we illustrate our analysis through the dispersion relations of two distinct unit cell models: (i) a resonant meta-barrier model composed of concrete and rubber, and (ii) a pure concrete box model. The mass and external volume of both elements are kept constant for better comparison. Following the approach outlined in Section 2.2.1, we constructed a finite element (FE) model in

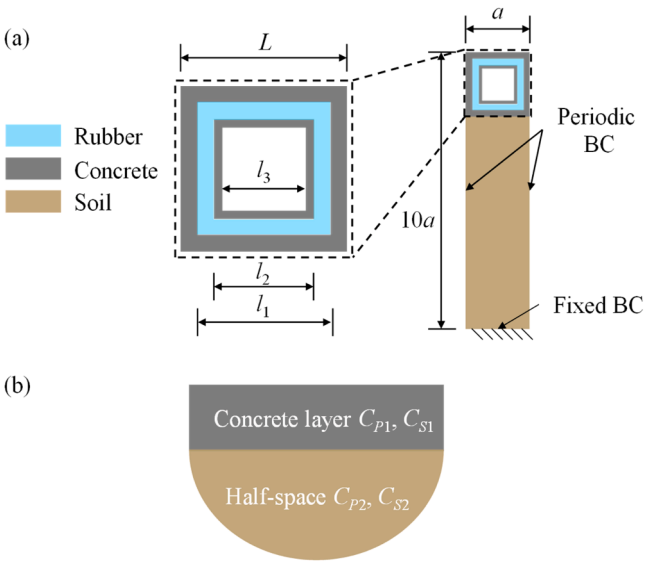

Fig. 6. Schematic of the analytical analysis model. (a) Unit cell model of resonant meta-barrier. (b) Equivalent layer model.

COMSOL and applied periodic boundary conditions to the left and right sides of the unit cell to determine the dispersion relation.

Using the material parameters displayed in Table 1, we show the dispersion curves for model (i) in the color-coded Fig. 7a. The horizontal lines indicate local resonance modes, as illustrated by mode shapes *B* - *D*. It is important to note that these resonance modes cannot propagate due to their null group velocity. All other eigenmodes lie above the sound line, as shown by the black dashed line in Fig. 7a and 7b, which corresponds to the shear velocity of the substrate. The region beyond the sound line is shaded in gray, indicating all possible bulk modes. Therefore, these modes are classified as bulk modes based on the sound line and the energy center parameter defined in Eq. (7). This observation aligns with our discussion in Section 3.1, indicating that the zero-frequency bandgap (ZFBG) in this model, shaded in light brown [42], arises from the configuration itself, a hard layer placed atop a soft substrate, rather than from the introduction of metamaterials.

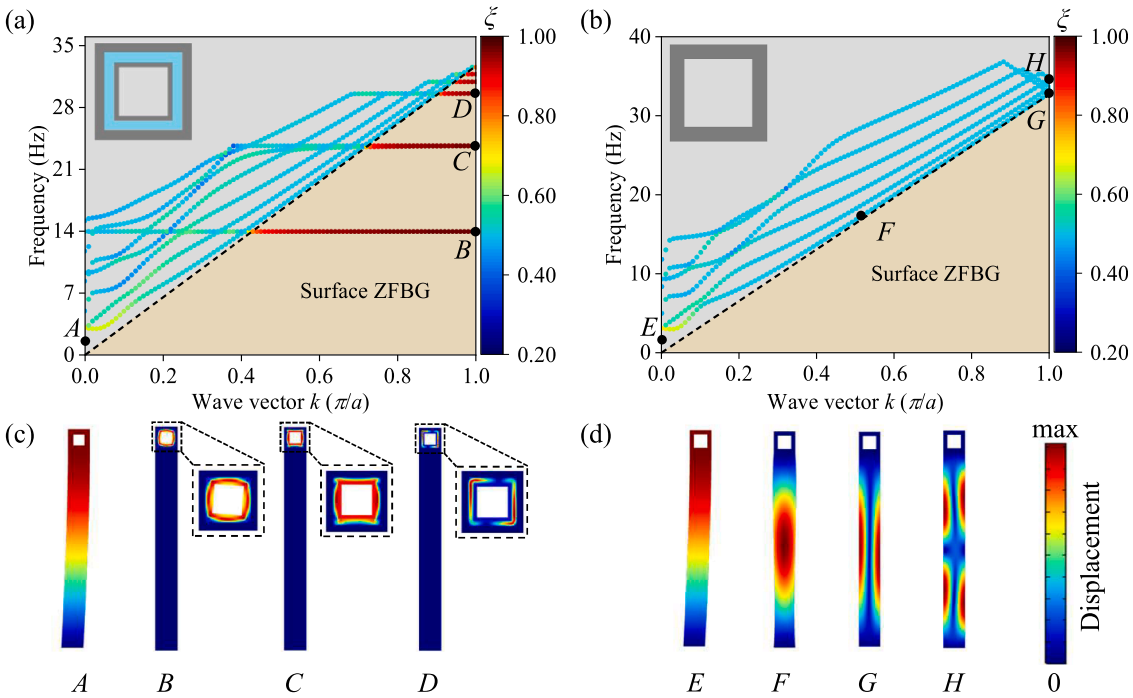

Fig. 7. Dispersion curve of (a) the meta-barrier model and (b) the concrete box model. Typical modes of (c) the meta-barrier model and (d) the concrete box model.

To further support this conclusion, we analyze the dispersion curve of model (ii), the pure concrete box unit cell. Using the same method, we present the color-coded dispersion curves in Fig. 7b. As anticipated, there are no local resonance modes, and all eigenmodes (represented as *E* to *H*) are bulk modes situated above the sound line. This finding also corresponds with our analysis in Section 3.1, where these bulk modes can be clearly identified by their mode shapes shown in Fig. 7d. Thus, a similar ZFBG can be achieved by simply placing a pure concrete layer on top of a soft half-space.

From the analysis of these two models, we conclude that the mechanism behind this surface ZFBG is not attributed to the unique bandgap properties of the meta-barrier element. Instead, it arises from the intrinsic characteristics of the model, which features a stiff layer placed over a half-space, leading to the absence of pure surface modes in the system.

3.2.2. *Frequency domain analysis*

To further elaborate on our analysis of the ZFBG revealed by the dispersion analysis, we conduct FE numerical simulations in the frequency domain. We utilize the same FE model shown in Fig. 3, replacing the bedrock with soil and the clamped barriers with 20 unit cells. Both unit-cell models (i) and (ii) will be investigated, along with a model consisting solely of soil for comparison.

The amplitude ratio spectra (ARS) of the meta-barrier and concrete box models are presented in Fig. 8a, indicated by dashed and solid lines, respectively. Notably, the presence of negative ARS in the considered frequency range confirms the existence of the surface ZFBG, consistent with the dispersion analysis above. Furthermore, the two curves are nearly identical, especially in the low-frequency range, suggesting that the effect of local resonance is negligible. This result reinforces the conclusion that the ZFBG is attributed to the

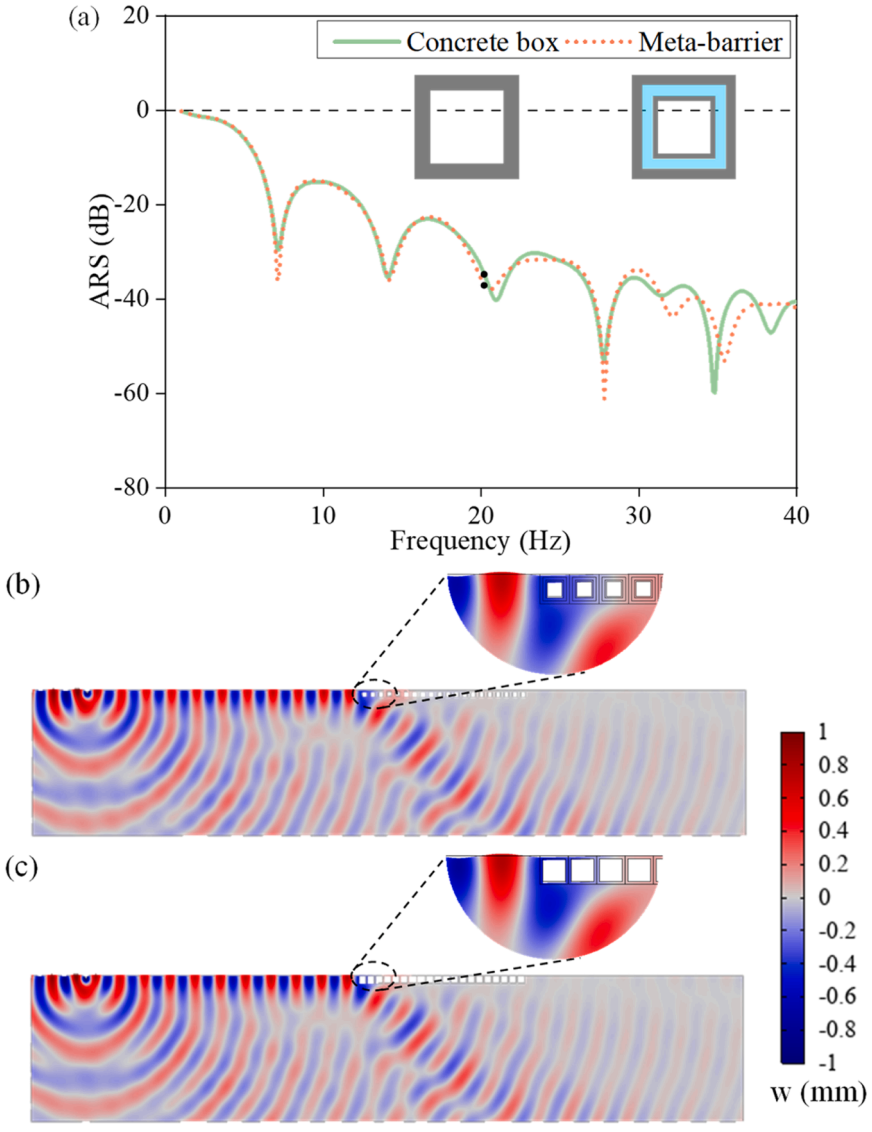

Fig. 8. Frequency domain results. (a) ARS spectrum. Vertical displacement field of (b) the meta-barrier model and (c) the concrete box model.

configuration of the upper hard layer rather than the metamaterials.

To further demonstrate that only bulk modes exist in models (i) and (ii), as predicted by both theoretical and numerical analyses, we present the wavefields for both models in Fig. 8b and 8c. As anticipated, the incident Rayleigh wave induced by a vertical harmonic point load, upon interacting with the meta-barriers and concrete boxes, is converted into bulk modes, indicating that pure Rayleigh wave propagation is prohibited in both models.

3.2.3. *Time domain analysis*

In parallel, we conduct time-dependent analyses on models (i) and (ii) to further illustrate our conclusions. Following the procedure outlined in Section 2.2.3, we apply a vertical excitation with a central frequency of 5 Hz, which falls within the ZFBG. The results are presented in Fig. 9.

As anticipated, the incident Rayleigh wave in both models (i) and (ii) is significantly attenuated compared to the reference pure soil model. Notably, the responses of models (i) and (ii) are identical, consistent with the results presented in Fig. 8a. Additionally, we show snapshots of the wavefields at 4.2 seconds in Fig. 9b and 9c. These results demonstrate that the incident Rayleigh waves are effectively

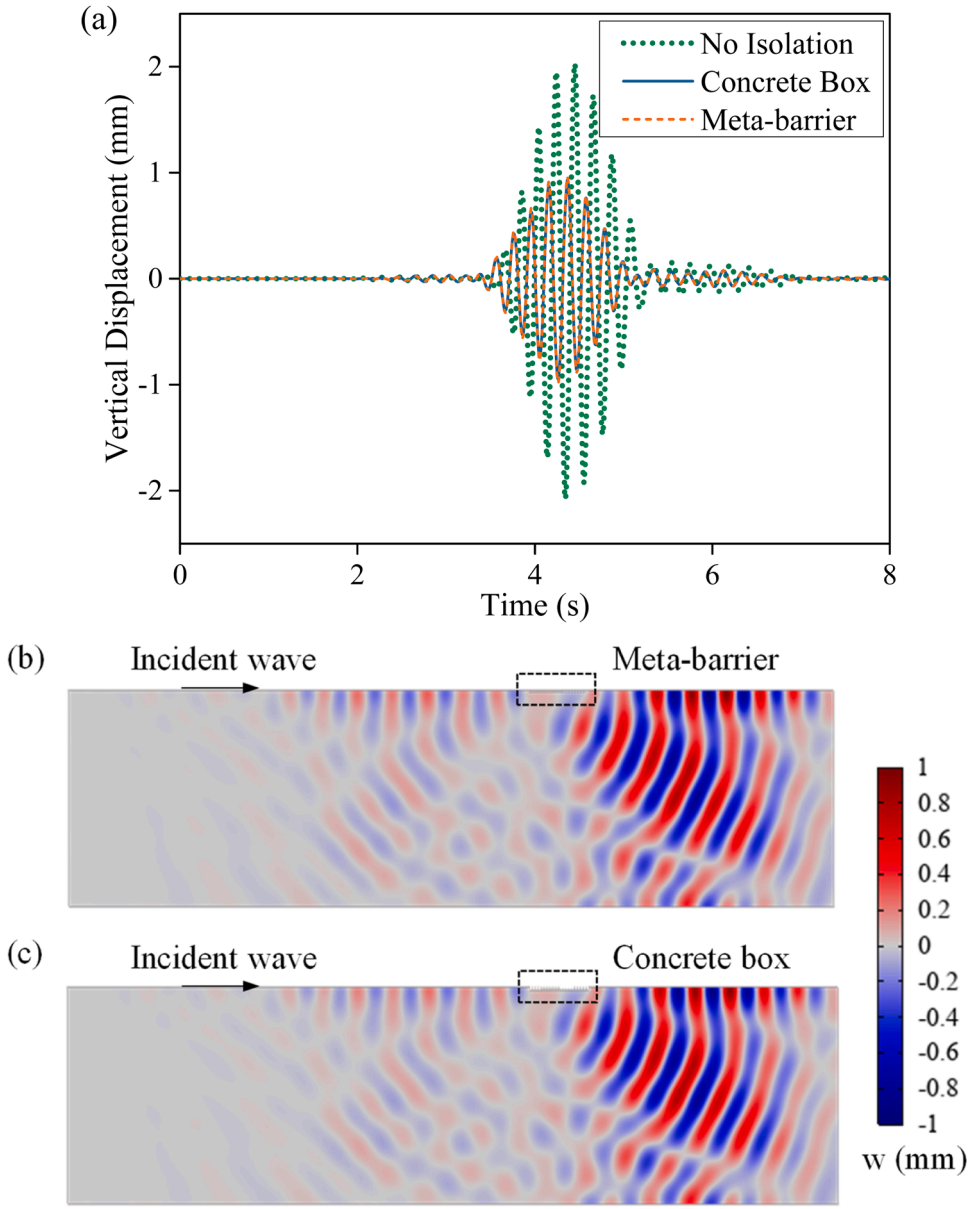

Fig. 9. Time domain results. (a) Vertical displacement time history. Vertical displacement field of (b) the meta-barrier model and (c) the concrete box model.

converted to bulk waves, the same phenomenon observed in the frequency domain in the previous section. These findings reinforce our conclusions regarding the surface ZFBG.

Overall, based on the above theoretical and numerical analysis, it is evident that the mechanism behind the surface ZFBG in the meta-barrier design arises from the absence of pure surface modes. This phenomenon is an intrinsic property of having a stiff upper layer atop a soft half-space, rather than stemming from the unique bandgap characteristics of the metamaterial itself. It is important to note that this observation also holds true for the gradient variation of unit cells, as elaborated in Appendix B.

4. Conclusion

The recent increase in seismic metamaterials designed for manipulating seismic surface waves has resulted in the development of several unit cells capable of achieving ultra-low-frequency and even zero-frequency bandgaps (ZFBGs). In this work, we investigate two representative models capable of achieving ZFBGs: the clamped barrier model and the resonant meta-barrier model. Through analytical and numerical analyses, we demonstrate that metamaterials are not a prerequisite for the formation of ZFBGs.

To illustrate this, we introduce a clamped barrier whose unit cell consists of a fly ash barrier clamped to bedrock and surrounding soil. We first propose a discrete spring-mass model that demonstrates the physical origin of the ZFBG as the formation of negative effective mass, resulting from the introduction of grounded springs. From a continuum model perspective, these grounded springs can be associated with a rigid foundation. Our numerical calculations of dispersion relationships, along with frequency and time domain simulations, reveal that both the clamped barrier model and the model of a homogeneous soil layer overlying bedrock can produce ZFBGs; notably, the latter does not qualify as a metamaterial. Thus, we claim that a rigid boundary condition is responsible for the formation of these types of ZFBGs. It should be noted that the width of the ZFBG may be influenced by the thickness of the top-layer soil, as discussed in Appendix C.

Furthermore, we investigated the dispersion relationship of a meta-barrier whose unit cell is composed of a rubber-coated concrete block embedded in a concrete matrix. For comparison, we also analyzed the dispersion relationship of a pure concrete box model without the core. Our findings indicate that, aside from a few resonant modes present in the meta-barrier, the dispersion relationships of both models are very similar, and neither supports pure surface wave modes. Note that the latter model is also not classified as a metamaterial. Through theoretical analysis and both frequency- and time-domain simulations, we demonstrate that the ZFBG in these models is determined by the intrinsic characteristics of a hard layer over a soft half-space, rather than being dominated by the resonant effects of metamaterial unit cells. Note also that the height of the unit cell also affects the ZFBG characters (see Appendix C).

However, this study has certain limitations that should be acknowledged. First, the analytical and numerical models assume linear elasticity, homogeneity, and isotropy for all materials, which may not fully capture the nonlinear, heterogeneous, and viscoelastic behavior of real-world soils, especially under large-strain conditions. Second, practical implementation challenges, such as construction tolerances, material durability, and environmental interactions (e.g., soil erosion, water saturation), were not considered, which could affect the long-term performance of seismic metamaterials. Finally, the conclusions are based on numerical and analytical results, and experimental validation under controlled or field conditions would further reinforce the findings.

Overall, we anticipate that our work on the mechanisms behind ZFBG generation will serve as a guide for designing and interpreting data from experimental or numerical tests on ground vibration control devices, such as wave barriers and seismic metamaterials.

CRediT authorship contribution statement

Jingyu Luo: Writing – original draft, Validation, Software, Investigation, Data curation. **Kaiming Bi:** Writing – review & editing, Supervision, Resources, Project administration, Funding acquisition, Formal analysis, Conceptualization. **Xingbo Pu:** Writing – review & editing, Supervision, Resources, Methodology, Investigation, Formal analysis, Conceptualization.

Declaration of competing interest

The authors declare that they have no known competing financial interests or personal relationships that could have appeared to influence the work reported in this paper.

Acknowledgments

The second author would like to acknowledge the partial support of the start-up fund (1-BDCR) from The Hong Kong Polytechnic University (PolyU). The third author acknowledges the support from the Joint Research Centre for Marine Infrastructure (A/C: 1-CEB0) at PolyU.

Appendix A. Shielding effect of the combined model

In this section, we present the shielding effect of the combined model, following the same approach used for the previous two types of seismic metamaterials. Fig. A1(a) depicts the schematic diagram and geometric parameters of the combined model, which consists of fly ash, rubber, concrete, and soil. The material used here is the same as the main text, whose properties are detailed in Table 1.

The dispersion relation of the combined model is shown in Fig. A1(b). As expected, the combined model exhibits a stop band with a

cut-off frequency of 3.6 Hz, indicating the formation of a zero-frequency band gap (ZFBG). This finding is the same as the clamped barrier model, indicating that the combined model can achieve the same shielding effect as the clamped barrier.

Similar to the resonant meta-barrier model, local resonance modes, represented by horizontal lines, are also observed in Fig. A1(b). Additionally, all other eigenmodes lie above the sound line, confirming the existence of the surface ZFBG. Therefore, the combined can achieve the same shielding effect as the resonant meta-barrier model. These results indicate that the two designs can be effectively combined to achieve a superimposed shielding effect.

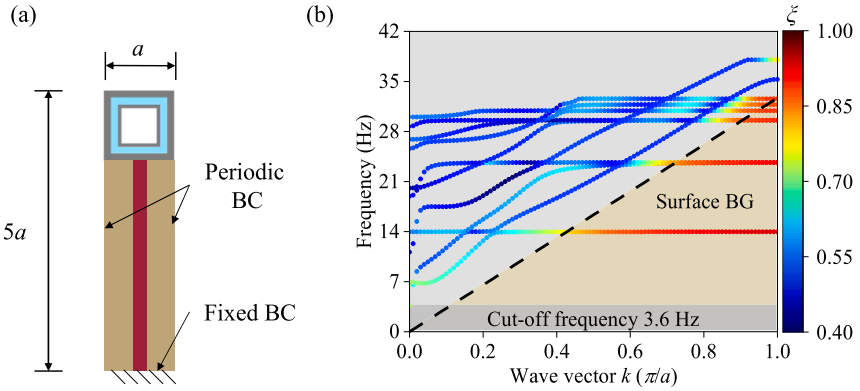

Fig. A1. Combined model: (a) Unit cell, (b) Dispersion curves.

Appendix B. Gradient meta-barrier model

To further demonstrate that ZFBG of meta-barriers is determined by the intrinsic characteristics of a hard layer over a soft half-space, we examine the ARS of two gradient metamaterial models as well, as illustrated in Figs. B1(a) and B1(b). In this appendix, we analyze the gradient effects of the height (denoted as h) of the meta-barrier model, with which varying from $0.525a$ to a in increments of $0.025a$. No other geometrical or mechanical parameters were changed except for the height of the meta-barrier. The models with gradually increasing and decreasing heights are referred to as $h+$ and $h-$, respectively. The frequency domain results for both gradient models are shown in Fig. B1(c). It can be seen that, although the shielding effect of the gradient models is slightly less effective than that of the periodic model, the presence of negative ARS within the examined frequency range reaffirms the existence of the surface ZFBG in both the $h+$ and $h-$ models. Additionally, the variation of the shielding effects between models with and without gradient can be explained by the geometric scattering effects, which controlled by the scattering area. Since the scattering area of the gradient model is smaller than that of the periodic model, its shielding effect os correspondingly less effective.

Overall, due to the outer concrete matrix, the gradient meta-barriers can be regarded as a gradient uniform concrete layer over a soft half-space, resulting in a full ZFBG similar to their periodic counterparts discussed in the main text."

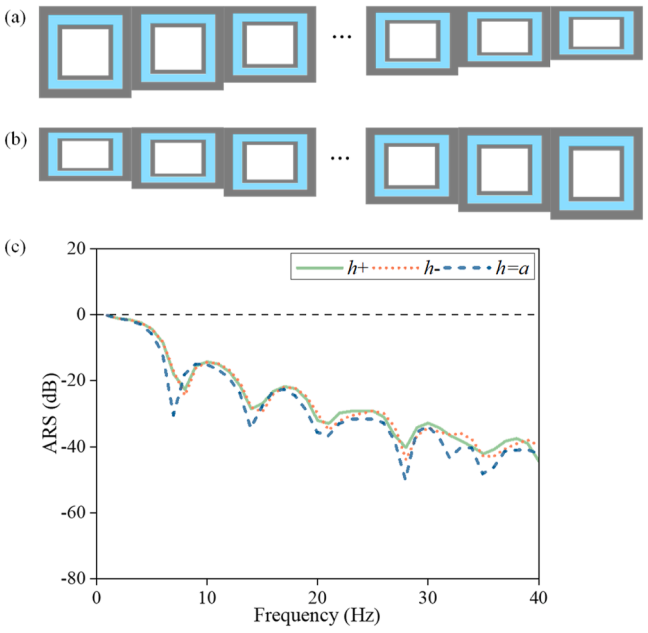

Fig. B1. Schematic diagram of gradient meta-barrier model: (a) *h*- model. (b) *h*+ model. (c) ARS spectrum of *h*-, *h*+ and *h*=*a* model.

Appendix C. Analysis of geometrical parameters on dispersion relations

To investigate the influence of the height of the barrier on the ZFBG, we propose a series of clamped barrier models with varying heights. Here, the height to distance ratio (*H/a)* varies from 0.5 to 10 with increments of 0.5. By analyzing the dispersion relations of clamped barrier models with different heights, we obtain the relationship between cut-off frequencies and the height to distance ratio. As shown in Fig. C1, the cut-off frequency decreases and approaches zero as the *H/a* increases. This can be explained by the fundamental structural dynamics: when the upper layer is extremely thin, the system exhibits high stiffness, which results in a relatively high natural frequency; Conversely, as the thickness of the upper layer increases, the stiffness of the system gradually diminishes, leading to a lower natural frequency. Overall, although the range of cut-off frequencies changes, ZFBG exists in all models, which reinforces our conclusions presented in the main text.

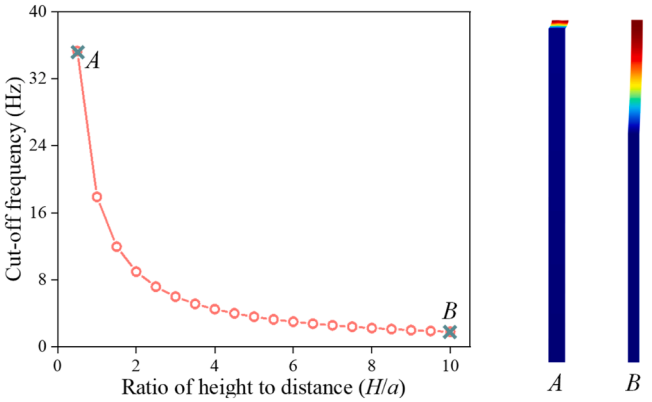

Fig. C1. The impact of *H/a* on the cut-off frequency of the clamped barrier model.

Similarly, we examine the effect of concrete layer thickness on the ZFBG characteristics. For simplicity, we only consider a void-free concrete layer on top of the soil layer. The dispersion relations of unit cell models with different thicknesses are shown in Fig. C2. The results show that as the thickness of the concrete layer decreases, the first-order mode transitions from bulk wave to surface wave. This evolution is visually evident in both the color-coded ξ parameter variations and mode shapes. Specifically, the mode shape insets (*A*-*H*) demonstrate that, when the thickness ratio (*H/a*) is less than 0.05, wave energy is predominantly concentrated at the surface. This phenomenon arises from diminished geometric scattering effects, which occurs when the wavelength significantly exceeds the characteristic dimensions of the scatterer (i.e., the overlying layer). Consequently, the thickness parameter becomes a critical design consideration for achieving ZFBG configurations in meta-barriers. Based on our parametric analysis, we recommend maintaining a minimum thickness ratio of $H/a \geq 0.05$ to ensure optimal performance.

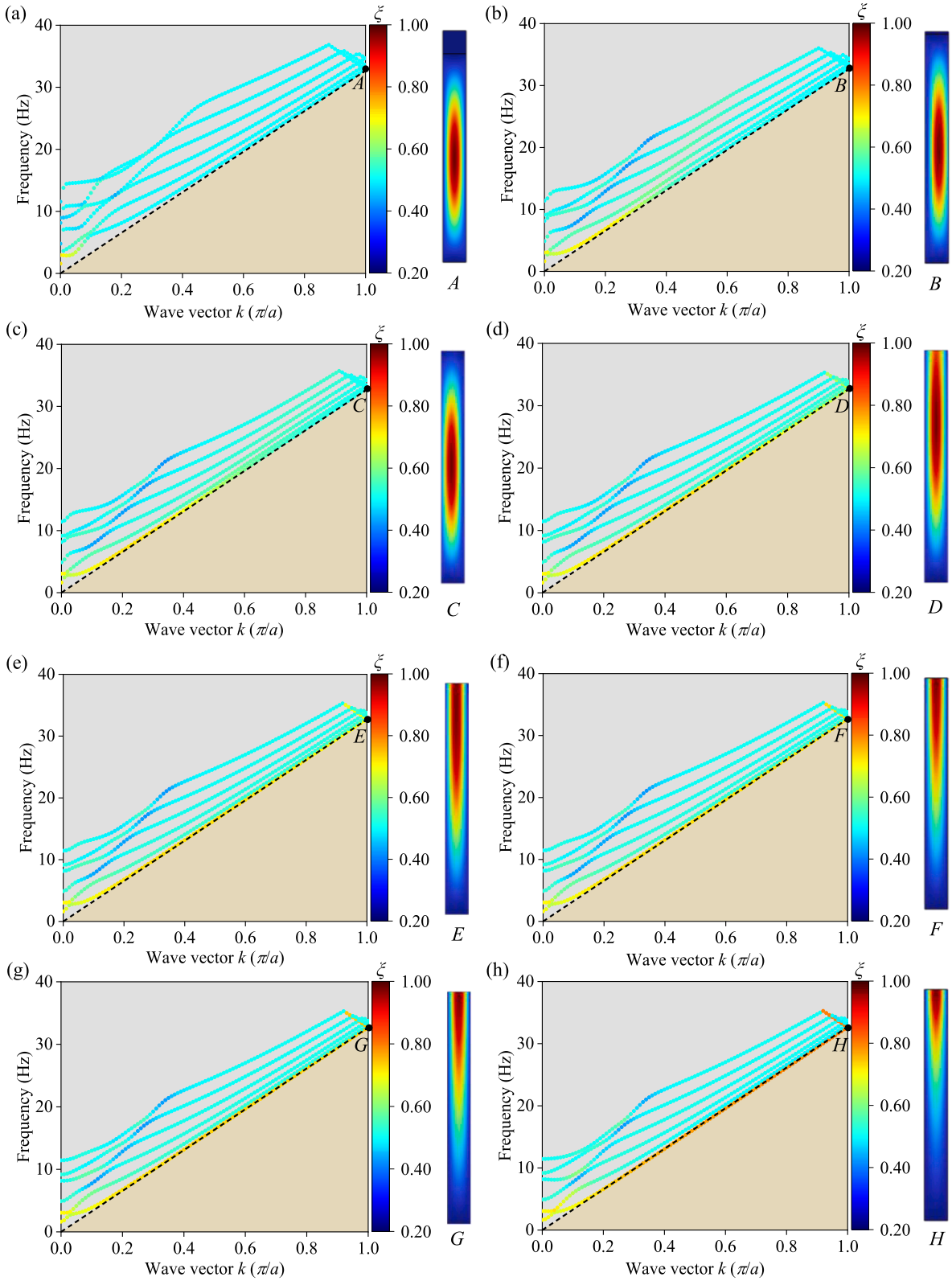

Fig. C2. The impact of H/a on dispersion curves of meta-barrier models: (a) H/a=1. (b) H/a=0.1. (c) H/a=0.05. (d) H/a=0.02. (e) H/a=0.015. (f) H/a=0.01. (g) H/a=0.005. (h) H/a=0.001.

Data availability

Data will be made available on request.

References

[1] Z. Tao, X. Ren, A.G. Zhao, et al., A novel auxetic acoustic metamaterial plate with tunable bandgap, Int. J. Mech. Sci. 226 (2022) 107414, https://doi.org/10.1016/j.ijmecsci.2022.107414.
[2] X.C. Teng, X. Ren, Y. Zhang, et al., A simple 3D re-entrant auxetic metamaterial with enhanced energy absorption, Int. J. Mech. Sci. 229 (2022) 107524, https://doi.org/10.1016/j.ijmecsci.2022.107524.
[3] Y. Jin, N. Fernez, Y. Pennec, et al., Tunable waveguide and cavity in a phononic crystal plate by controlling whispering-gallery modes in hollow pillars, Phys. Rev. B 93 (5) (2016) 054109, https://doi.org/10.1103/PhysRevB.93.054109.
[4] Y. Jin, R. Kumar, O. Poncelet, et al., Flat acoustics with soft gradient-index metasurfaces, Nat. Commun. 10 (1) (2019) 143, https://doi.org/10.1038/s41467-018-07990-5.
[5] Y. Jin, X. Fang, Y. Li, et al., Engineered Diffraction Gratings for Acoustic Cloaking, Phys. Rev. Appl. 11 (1) (2019) 011004, https://doi.org/10.1103/PhysRevApplied.11.011004.
[6] C.W.L. Muhammad, J.N. Reddy, Built-up structural steel sections as seismic metamaterials for surface wave attenuation with low frequency wide bandgap in layered soil medium, Eng. Struct. 188 (2019) 440–451, https://doi.org/10.1016/j.engstruct.2019.03.046.
[7] Muhammad, C.W. Lim, From photonic crystals to seismic metamaterials: a review via phononic crystals and acoustic metamaterials, Arch. Comput. Methods Eng. 29 (2) (Mar. 2022) 1137–1198, https://doi.org/10.1007/s11831-021-09612-8.
[8] Z. Chen, G. Wang, C.W. Lim, Artificially engineered metaconcrete with wide bandgap for seismic surface wave manipulation, Eng. Struct. 276 (2023) 115375, https://doi.org/10.1016/j.engstruct.2022.115375.
[9] S. Brûlé, E.H. Javelaud, S. Enoch, et al., Experiments on seismic metamaterials: molding surface waves, Phys. Rev. Lett. (2014), https://doi.org/10.1103/PhysRevLett.112.133901.
[10] L. Meng, Z. Shi, S. Hao, et al., Filtering property of periodic in-filled trench barrier for underground moving loads, Constr. Build. Mater. 400 (2023) 132655, https://doi.org/10.1016/j.conbuildmat.2023.132655.
[11] Z. Shi, Z. Cheng, J. Wu, Numerical evaluation of the effectiveness of periodic wave barriers in pre-stressed saturated soil, J. Vib. Eng. Technol. 11 (8) (2023) 4269–4279, https://doi.org/10.1007/s42417-022-00814-3.
[12] A. Ni, Z. Shi, Q. Meng, et al., A novel buried periodic in-filled pipe barrier for Rayleigh wave attenuation: numerical simulation, experiment and applications, Eng. Struct. 297 (2023) 116971, https://doi.org/10.1016/j.engstruct.2023.116971.
[13] X. Pu, Z. Shi, Surface-wave attenuation by periodic pile barriers in layered soils, Constr. Build. Mater. 180 (2018) 177–187, https://doi.org/10.1016/j.conbuildmat.2018.05.264.
[14] K. Zhang, J. Luo, F. Hong, et al., Seismic metamaterials with cross-like and square steel sections for low-frequency wide band gaps, Eng. Struct. 232 (Apr. 2021) 111870, https://doi.org/10.1016/j.engstruct.2021.111870.
[15] L. Gao, C. Cai, C.M. Mak, et al., Surface wave attenuation by periodic hollow steel trenches with Bragg band gap and local resonance band gap, Constr. Build. Mater. 356 (2022) 129289, https://doi.org/10.1016/j.conbuildmat.2022.129289.
[16] Z.Y. Liu, X.X. Zhang, Y.W. Mao, et al., Locally resonant sonic materials, Science 289 (5485) (2000) 1734–1736, https://doi.org/10.1126/science.289.5485.1734.
[17] Y. Liu, X. Shen, X. Su, et al., Elastic Metamaterials With Low-Frequency Passbands Based on Lattice System With On-Site Potential, J. Vib. Acoust.-Trans. ASME 138 (2) (Apr. 2016) 021011, https://doi.org/10.1115/1.4032326.
[18] F. Zeighami, A. Palermo, A. Marzani, Rayleigh waves in locally resonant metamaterials, Int. J. Mech. Sci. 195 (2021) 106250, https://doi.org/10.1016/j.ijmecsci.2020.106250.
[19] A. Colombi, Forests as a natural seismic metamaterial: Rayleigh wave bandgaps induced by local resonances, Sci. Rep. 6 (1) (2016) 19238, https://doi.org/10.1038/srep19238.
[20] Y. Zeng, Y. Xu, K. Deng, et al., A broadband seismic metamaterial plate with simple structure and easy realization, J. Appl. Phys. 125 (22) (2019) 224901, https://doi.org/10.1063/1.5080693.
[21] Y. Zeng, S.-Y. Zhang, H.-T. Zhou, et al., Broadband inverted T-shaped seismic metamaterial, Mater. Design 208 (2021) 109906, https://doi.org/10.1016/j.matdes.2021.109906.
[22] J. Xiong, F. Ren, S. Li, et al., A study on low-frequency vibration mitigation by using the metamaterial-tailored composite concrete-filled steel tube column, Eng. Struct. 305 (Apr. 2024) 117673, https://doi.org/10.1016/j.engstruct.2024.117673.
[23] A. Colombi, D. Colquitt, P. Roux, et al., A seismic metamaterial: The resonant metawedge, Sci. Rep. 6 (1) (2016) 27717, https://doi.org/10.1038/srep27717.
[24] G.J. Chaplain, J.M. De Ponti, A. Colombi, et al., Tailored elastic surface to body wave Umklapp conversion, Nat. Commun. 11 (1) (2020) 3267, https://doi.org/10.1038/s41467-020-17021-x.
[25] X. Wang, S. Wan, Y. Nian, et al., Periodic in-filled pipes embedded in semi-infinite space as seismic metamaterials for filtering ultra-low-frequency surface waves, Constr. Build. Mater. 313 (2021) 125498, https://doi.org/10.1016/j.conbuildmat.2021.125498.
[26] X. Wang, S. Wan, P. Zhou, et al., Topology optimization of periodic pile barriers and its application in vibration reduction for plane waves, Soil Dyn. Earthquake Eng. 153 (2022) 107119, https://doi.org/10.1016/j.soildyn.2021.107119.
[27] X. Wang, S. Wan, P. Zhou, et al., Vibration mitigation in porous soil using periodic rock-socketed pile barriers, Soil Dyn. Earthquake Eng. 171 (2023) 107956, https://doi.org/10.1016/j.soildyn.2023.107956.
[28] Y. Achaoui, T. Antonakakis, S. Brule, et al., Clamped seismic metamaterials: ultra-low frequency stop bands, New J. Phys. 19 (2017) 063022, https://doi.org/10.1088/1367-2630/aa6e21.
[29] Y. Chen, F. Qian, F. Scarpa, et al., Harnessing multi-layered soil to design seismic metamaterials with ultralow frequency band gaps, Mater. Des. 175 (2019) 107813, https://doi.org/10.1016/j.matdes.2019.107813.
[30] T.V. Varma, B. Ungureanu, S. Sarkar, et al., The Influence of Clamping, Structure Geometry, and Material on Seismic Metamaterial Performance, Front. Mater. 8 (2021) 603820, https://doi.org/10.3389/fmats.2021.603820.
[31] H.K. Maheshwari, P. Rajagopal, Novel locally resonant and widely scalable seismic metamaterials for broadband mitigation of disturbances in the very low frequency range of 0-33 Hz, Soil Dyn. Earthq. Eng. 161 (2022) 107409, https://doi.org/10.1016/j.soildyn.2022.107409.
[32] Y. Zeng, P. Peng, Q.-J. Du, et al., Subwavelength seismic metamaterial with an ultra-low frequency bandgap, J. Appl. Phys. 128 (1) (2020) 014901, https://doi.org/10.1063/1.5144177.
[33] N. Shi, H. Liu, L. Wang, et al., Double-gradient seismic metamaterials with zero-frequency bandgap characteristic in a layered soil medium, EPL 144 (2) (2023) 20001, https://doi.org/10.1209/0295-5075/ad04ee.
[34] B.M. Das, Fundamentals of soil dynamics, Elsevier, New York, 1983.
[35] A. Martowicz, M. Ruzzene, W.J. Staszewski, et al., Out-of-plane elastic waves in 2d models of solids: a case study for a nonlocal discretization scheme with reduced numerical dispersion, Math. Probl. Eng. 2015 (2015) 584081, https://doi.org/10.1155/2015/584081.
[36] F. Farzbod, M.J. Leamy, Analysis of bloch's method and the propagation technique in periodic structures, J. Vib. Acoust. 133 (3) (2011) 031010, https://doi.org/10.1115/1.4003202.
[37] S. Yao, X. Zhou, G. Hu, Investigation of the negative-mass behaviors occurring below a cut-off frequency, New J. Phys. 12 (10) (Oct. 2010) 103025, 2010101503130400.

[38] J. Mei, Z. Liu, J. Shi, et al., Theory for elastic wave scattering by a two-dimensional periodical array of cylinders: an ideal approach for band-structure calculations, Phys. Rev. B 67 (24) (2003) 245107, https://doi.org/10.1103/PhysRevB.67.245107.
[39] T.-X. Ma, L. Cao, Complex dispersion analysis of true and pseudo surface waves propagating in two-dimensional viscoelastic seismic metamaterials, AIP Adv. 14 (1) (2024) 015219, https://doi.org/10.1063/5.0187232.
[40] F. Song, G.L. Huang, G.K. Hu, Online Guided Wave-Based Debonding Detection in Honeycomb Sandwich Structures, AIAA J. 50 (2) (2012) 284–293, https://doi.org/10.2514/1.J050891.
[41] J.D. Achenbach, Wave propagation in elastic solids, in: North-Holland Series in Applied Mathematics and Mechanics, v. 16, North-Holland Pub. Co., Amsterdam, 1973.
[42] P. Li, F. Yang, M. Zhao, et al., A new seismic metamaterial design with ultra-wide low-frequency wave suppression band utilizing negative Poisson's ratio material, Eng. Struct. 319 (2024) 118821, https://doi.org/10.1016/j.engstruct.2024.118821.